




# A new trial for lightweight MXene hybrid aerogels with high electromagnetic interference shielding performance

Xuanhe Ru<sup>1</sup>, Haiyang Li<sup>1</sup>, Yiwen Peng<sup>1</sup>, Zewen Fan<sup>1</sup>, Junjie Feng<sup>1</sup>, Lei Gong<sup>2,3</sup>, Zhenguo Liu<sup>2,3</sup>, Yanhui Chen<sup>1,\*</sup> , and Qiuyu Zhang<sup>1</sup>

<sup>1</sup>School of Chemistry and Chemical Engineering, Shaanxi Key Laboratory of Macromolecular Science and Technology, Key Laboratory of Special Functional and Smart Polymer Materials of Ministry of Industry and Information Technology, Northwestern Polytechnical University, Xi'an 710072, China

<sup>2</sup>Ningbo Institute of Northwestern Polytechnical University, Ningbo 315103, China

<sup>3</sup>Institute of Flexible Electronics, Northwestern Polytechnical University, Xi'an 710072, China

**Received:** 1 November 2021

**Accepted:** 13 December 2021

**Published online:**

23 January 2022

© The Author(s), under exclusive licence to Springer Science+Business Media, LLC, part of Springer Nature 2021

## ABSTRACT

Lightweight and conductive MXene/reduced graphene oxide (MX/rGO) aerogels have great potential in the field of electromagnetic interference (EMI) shielding. To achieve better EMI shielding performance, some fabrication ways and reduction methods for MX/rGO aerogels have been tried, but still far from the expectation. Herein, we develop a feasible technique to fabricate MX/rGO aerogels, i.e., unidirectional-freezing and subsequent mild chemical reduction treatment using the mixture of hydroiodic acid and acetic acid glacial. The lightweight MX/rGO hybrid aerogel with the weight ratio of MX/rGO 5:5 demonstrates superior electrical conductivity (467 S/m) and EMI shielding performance (57.67 dB). When the weight ratio of MX/rGO becomes 3:5, the EMI shielding performance reaches as high as 21,427 dB cm<sup>2</sup> g<sup>-1</sup>, which is almost higher than the EMI shielding performance of the 3D aerogels reported by the current available literature. The MX/rGO aerogels developed in this paper shows the great application potential in protecting the wearable and intelligent devices.

## 1 Introduction

With the advent of the 5G era, electronic devices are becoming more widely used in our daily life. As one of the most influential factors for the electronical

devices, the electromagnetic interference (EMI) not only can cause disturbances or failure of the electronic system, but also harm the human health. Most of the conventional EMI shielding materials consist of metals (e.g. Cu or Al). However, the limitations of metallic materials are also obvious, such as corrosion

Address correspondence to E-mail: yanhuichen@nwpu.edu.cn

susceptibility, high density and poor processability. Therefore, a lot of nonmetallic materials, like carbon nanotubes (CNTs) [1] and reduced graphene oxide (rGO) [2], have been developed to absorb electromagnetic waves. Nonetheless, the EMI performance of these materials still falls short of expectations.

MXene with a formula of  $M_{n+1}X_nT_x$ , where M represents transition metal, X represents C and N, and T represents a terminating functional group, such as  $-O$ ,  $-OH$ , and  $-F$ , is a new family of two-dimensional (2D) transition metal carbides or nitrides. Different from the inert and hydrophobic graphene, MXene demonstrates diversiform surface chemistry and layered structure, which allows itself to be applied in various areas. Up to now, MXene has been intensively exploited for various potential applications, such as super-capacitors [3–5], batteries [6, 7] and EMI shielding material [8–10], due to its high aspect ratios, excellent mechanical and electrical properties. Especially, its application in the EMI shielding field gets more and more attention from academia. Shahzad et al. [11] successfully prepared  $Ti_3C_2T_x$  for the first time, and their team reported a 45- $\mu\text{m}$ -thick  $Ti_3C_2T_x$  film with EMI shielding effectiveness of 92 dB. Jin et al. [12] obtained a PVA/MXene film featured with alternating multilayered structure via multilayered casting. The 27- $\mu\text{m}$ -thick multilayered film (containing 19.5 wt% MXene) exhibited a high conductivity of 716 S/m and a maximum EMI SE of 44.4 dB.

Currently, the lightweight and flexible EMI shielding materials with high-performance 3D porous network are in high demand, especially in the field of smart electronic devices and aerospace [13, 14]. Some researchers have thus tried to assemble 2D MXene into a 3D porous network structure, in order to further improve the EMI shielding performance [15–17]. Zhao et al. [18] used a sacrificial template method to construct flexible 3D macroporous MXene films. Liu et al. [19] successfully fabricated the MXene foam by hydrazine-induced foaming process, and obtained a lightweight and durable MXene foam. Due to the porous structure, the EMI shielding effectiveness of MXene foam reached about 70 dB, compared to its unfoamed counterpart (53 dB).

However, it is difficult to directly construct a freestanding, flexible, and 3D porous structure of MXene sheets, owing to their weak interface interaction [20]. Generally, MXene sheets can be

interconnected and bridged to form a robust 3D structure by introducing polymers or additives as a linking agent [21]. Xu et al. [22] reported a composite foam constructed by  $Ti_2CT_x$  and PVA, the specific shielding effectiveness reached up to 5136 dB  $\text{cm}^2 \text{g}^{-1}$  with 0.15 vol% filler content. Zhou et al. [23] used sodium alginate as building blocks for the ultrathin  $Ti_3C_2T_x$ /sodium alginate aerogel films with a sponge-like structure. The aerogel films presented excellent EMI shielding effectiveness (54.3 dB).

Apart from that, graphene oxide (GO), with hydrophobic basal plane and hydrophilic edges, possesses an outstanding dispersibility and controllable gelation capability [24, 25]. Due to the unique amphiphilic structure and properties of GO, Zhao et al. [10] demonstrated a GO-assisted hydrothermal assembly approach to construct 3D  $Ti_3C_2T_x$  porous architectures, where GO sheets act as a gelation agent to help MXene form 3D structure. Fan et al. [9] developed an approach to fabricate a lightweight MXene/graphene hybrid foam by freeze-drying and heat reduction treatment. Nevertheless, the whole preparation process of MXene/rGO hybrid aerogels, including hydrothermal treatment and dialysis, is to some extent cumbersome and energy-consuming. Therefore, new approaches should be developed to optimize the preparation process of MXene/rGO hybrid aerogels.

It has been reported that HI and HAc mixture can effectively reduce GO and help rGO to gain high conductivity [5, 26]. And the chemical treatment is mild for MXene compared to the heat reduction treatment [20]. Hence, we used HI and HAc mixture to reduce the  $Ti_3C_2T_x$  MXene/GO hybrid aerogel, by way of unidirectional-freezing and freeze-drying. The mild chemical treatment allows GO to tightly connect the MXene flakes into a robust 3D porous structure and at the same time to effectively reduce GO and avoid the oxidation of MXene. Therefore, the electrical conductivity and the EMI SE of the hybrid aerogel can reach up to 467 S  $\text{m}^{-1}$  and 57.67 dB, which are far higher than those of the rGO aerogels. Moreover, the lightweight (0.0053 g  $\text{cm}^{-3}$ ) hybrid aerogel shows an outstanding EMI shielding effectiveness of 21,427 dB  $\text{cm}^2 \text{g}^{-1}$ . Our new trial to conduct a MXene/rGO 3D porous structure with high EMI shielding performance is simple, energy-saving as well as feasible.

## 2 Experiment

### 2.1 Materials

Ti<sub>3</sub>AlC<sub>2</sub> powders were purchased from Jilin 11 Technology Co., Ltd., GO powders from Suzhou Graphenechina Co., Ltd., lithium fluoride (LiF, 99.9%) from Aladdin, and hydrochloric acid (HCl, 37%) were purchased from Chengdu Chron Chemicals Co., Ltd. The solution of hydroiodic acid (HI) was obtained from Macklin, and acetic acid glacial (HAc) was obtained from Guangdong Guanghua Sci-Tech Co., Ltd. All materials were used without further purification.

### 2.2 Preparation of Ti<sub>3</sub>C<sub>2</sub>T<sub>x</sub>

Ti<sub>3</sub>C<sub>2</sub>T<sub>x</sub> was obtained by selectively etching Al species from the MAX phase (Ti<sub>3</sub>AlC<sub>2</sub>). In a typical process, 1 g of LiF was dissolved in 20 mL of 9 M HCl in a Teflon vessel, then 1 g of Ti<sub>3</sub>AlC<sub>2</sub> powder was added slowly when stirring at 35 °C and the reaction went on for 24 h. Subsequently, the suspension was washed by the deionized water and centrifuged at 3500 rpm for several times, until the pH reached approximately 6.0. Furthermore, the suspension was sonicated for 1 h followed by centrifugation at 3500 rpm for 1 h; eventually Ti<sub>3</sub>C<sub>2</sub>T<sub>x</sub> MXene was obtained after freeze-drying. The characterization of the Ti<sub>3</sub>C<sub>2</sub>T<sub>x</sub> is all displayed in Fig. S1 of Supporting Information, which proves the successful fabrication of the Ti<sub>3</sub>C<sub>2</sub>T<sub>x</sub> nanosheets.

### 2.3 Fabrication of MX/rGO hybrid aerogel

Firstly, the prepared MXene was directly mixed with GO dispersion (4 mL, 5 mg mL<sup>-1</sup>), and then sonicated for about 10 min to obtain a homogeneous MXene/GO solution. Secondly, the mixed solution was poured into a homemade container with a copper base and put it into liquid nitrogen for the unidirectional freezing. After freeze-drying, the prepared MXene/GO (MX/GO) hybrid aerogels were immersed in a mixture of HI and HAc (20 mL, volume ratio is 1:2) for 20 min at room temperature and then heated at 60 °C for 1 h to reduce the GO. Finally, the obtained MX/rGO aerogels were washed several times with ethanol and water alternately to completely remove the rest of the acid and then freeze-drying again. For simplification, the MX/rGO

aerogels with different weight ratios (i.e., 0:5, 1:5, 2:5, 3:5, 4:5 and 5:5) were donated as MX/rGO-0, MX/rGO-1, MX/rGO-2, MX/rGO-3, MX/rGO-4 and MX/rGO-5, respectively. The fabrication procedure of the materials is shown in Fig. 1. Besides, the control samples with random structure were also obtained by directly pouring the mixture of MXene and GO in the petri dish followed by the freezing processing, while keeping the rest of the procedure the same.

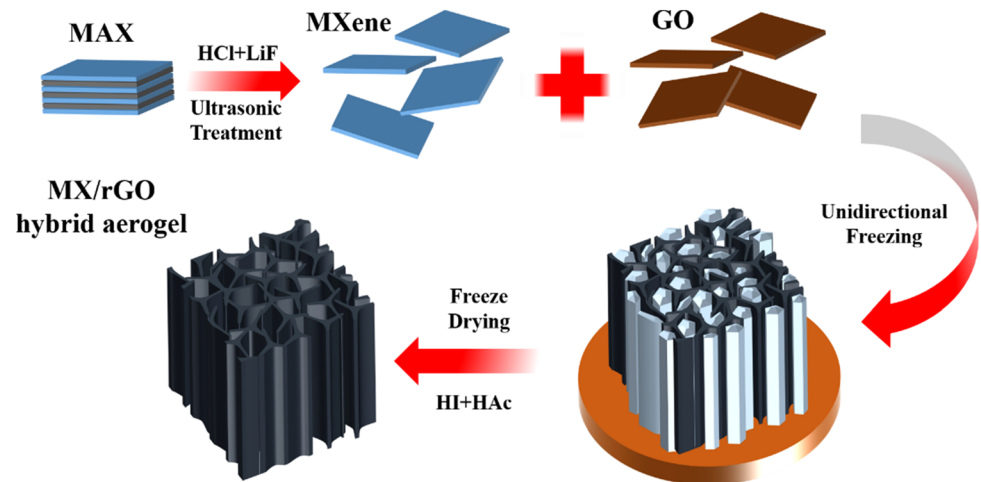
### 2.4 Characterization

Fourier transform infrared spectra (FTIR) of the samples were performed with a Bruker Tensor 27 equipment (Bruker Corp., Germany) at 4000–400 cm<sup>-1</sup> frequency range. XPS analyses of the samples were carried out by PHI5400 device (PE Corp., England). XRD of the samples was performed on a Shimadzu-7000 type X-ray diffraction (Cu K<sub>α</sub>, λ = 0.154 nm, Shimadzu, Japan). Raman spectrum was carried out by a WITec Alpha300R. SEM images of the samples were carried out on a Verios G4 XHR equipment (Thermo Fisher Scientific Corp., USA) at an accelerating voltage of 10 kV. TEM images of the samples were collected on a Talos F200X/TEM microscope (FEI Co., USA). AFM images of the samples were captured by a Dimension Fast Scan AFM (Bruker Corp., USA). Electrical conductivity (σ) values of the samples were measured by RTS-8 (Guangzhou Four Probes Technology Corp., China). EMI shielding parameters of the samples over the X-band frequency range (8.2–12.4 GHz) were measured on a MS4644A Vector Network Analyzer (Anritsu Corp., Japan) by wave-guide method according to ASTM D5568-08, and the corresponding size is 22.86 mm × 10.16 mm. It is worth noting that the test direction of electromagnetic radiation is set to be perpendicular to the growth direction unless specified. The reflection (R), transmission (T), and absorption (A) coefficients were obtained by calculating the scattering parameters (S<sub>11</sub> and S<sub>21</sub>). The total electromagnetic interference shielding efficiency (SE<sub>T</sub>), electromagnetic interference absorption (SE<sub>A</sub>) and electromagnetic interference reflection (SE<sub>R</sub>) can be obtained by Eqs. 1–6 [27].

$$R + A + T = 1 \quad (1)$$

$$R = |S_{11}|^2 = |S_{21}|^2 \quad (2)$$

**Fig. 1** Schematic illustration of the fabrication process of MX/rGO hybrid aerogels



$$T = |S_{12}|^2 = |S_{21}|^2 \quad (3)$$

$$SE_R = 10 \log \left( \frac{1}{1-R} \right) \quad (4)$$

$$SE_A = 10 \log \left( \frac{1-R}{T} \right) \quad (5)$$

$$SE_T = SE_R + SE_A + SE_M \quad (6)$$

The  $SE_R$  is related to the impedance mismatch between air and the absorber, while the  $SE_A$  is resulted from the energy dissipation of electromagnetic radiation. The  $SE_M$  is induced by the scattering effect of homogeneity in the material and it can be neglected when  $SE_A > 10$  dB [28].

To compare the effectiveness of shielding materials equitably, the density of the materials were also taken into account. The related equation was described as:

$$SSE = \frac{SE_T}{\rho} \quad (7)$$

### 3 Results and discussion

#### 3.1 Characterization of the MX/rGO hybrid aerogels

Selective FTIR spectra of MXene, GO and MX/rGO hybrid aerogels are presented in Fig. 2a. All the FTIR spectra of MX/rGO hybrid aerogels are displayed in Fig. S2. Peaks of GO at  $3408 \text{ cm}^{-1}$ ,  $1727 \text{ cm}^{-1}$ ,  $1224 \text{ cm}^{-1}$  and  $1052 \text{ cm}^{-1}$  are assigned to the characteristic absorption of O–H, C=O, C–O–C and C–OH group, respectively [29]. For MX/rGO hybrid

aerogels, many functional groups on the GO surface have been reduced after the chemical treatment, although there are two remaining shallow characteristic peaks locating in  $3408 \text{ cm}^{-1}$  and  $1727 \text{ cm}^{-1}$  in the FTIR spectra, corresponding to O–H, C=O group, respectively. As the MXene content increases, these two peaks get weaker and weaker. The successful removal of most oxygen-containing groups proves the efficient reduction of GO by the HI and HAC mixture. The efficient reduction of GO predicts its good electrical conductivity, and will contribute to the electromagnetic shielding performance of MX/rGO hybrid aerogels.

The presence of both MXene and rGO in MX/rGO hybrid aerogel is further confirmed by comparing the XRD patterns (Fig. 2b). MX/rGO-5 and MX/rGO-0 possess the same peak at  $25.1^\circ$ , which is ascribed to rGO [5]. The (002) peak of MX/rGO-5 at  $6.7^\circ$  indicates the well-preserved structure of MXene sheets after the chemical reduction treatment, and the (002) peak slightly shifts to the right compared to MXene, indicating the decrease of interlayer spacing, maybe caused by the stacking in the aerogel.

Raman spectra of MXene, MX/rGO-0 and MX/rGO-5 hybrid aerogels are shown in Fig. 2c. All the Raman spectra of MX/rGO hybrid aerogels are displayed in Fig. S3. The characteristic peaks of MXene are shown in the left part of Fig. 2c. The peaks at  $198$  and  $719 \text{ cm}^{-1}$  are  $A_{1g}$  symmetry out-of-plane vibrations of Ti and C atoms, respectively, while the peaks of  $E_g$  group vibrations appear at  $283$ ,  $371$  and  $621 \text{ cm}^{-1}$ , including in-plane shearing vibrations of Ti, C and surface functional group on MXene [30]. The similar patterns of MX/rGO-5 and MXene

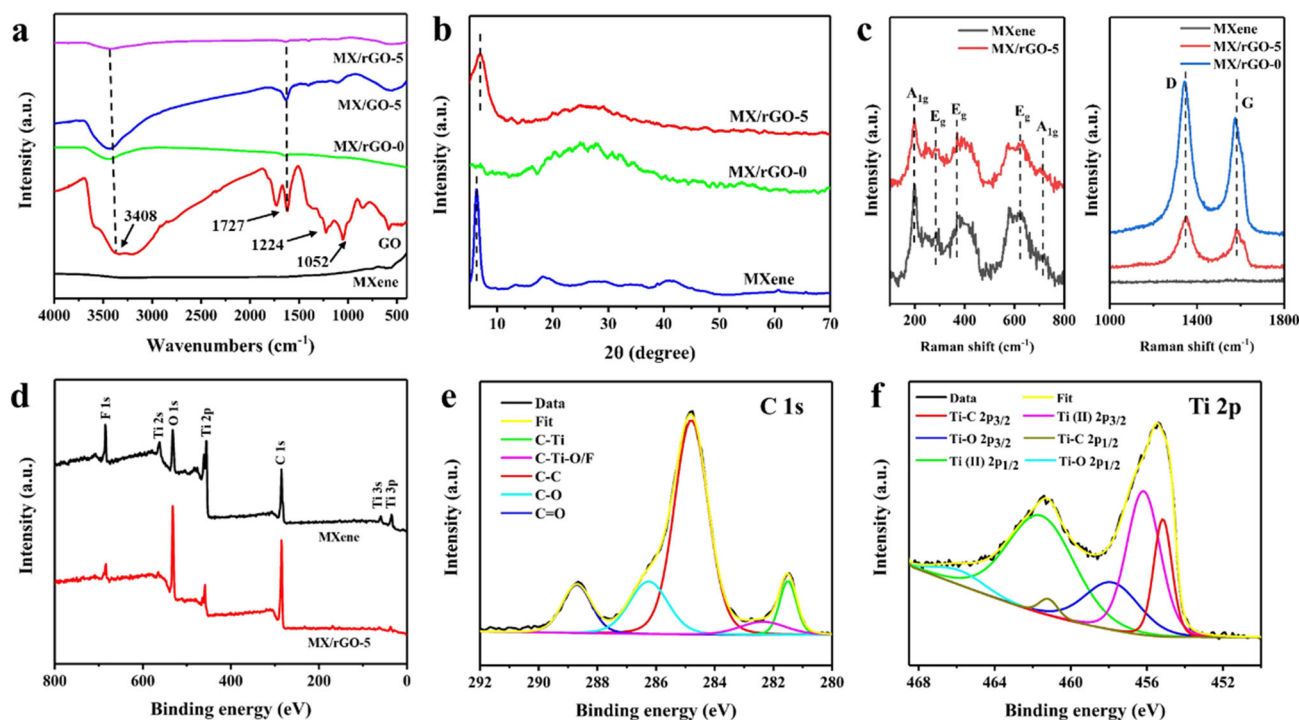


**Fig. 2** **a** FTIR spectra of MXene, GO, MX/rGO-5 and MX/rGO-5. **b** XRD patterns of MXene, MX/rGO-0 and MX/rGO-5. **c** Raman spectra of MXene, MX/rGO-0 and MX/rGO-5. **d** XPS spectra of

MXene and MX/rGO-5. High-resolution **e** C 1s and **f** Ti 2p spectra of MX/rGO-5

demonstrate the presence of MXene in MX/rGO-5 hybrid aerogel. In the right part, the distinct D and G bands of MX/rGO-0 and MX/rGO-5 indicate the presence of rGO in MX/rGO-5 hybrid aerogel. In summary, MXene and rGO are successfully combined in MX/rGO-5 hybrid aerogel.

To further ascertain the coexistence of MXene and rGO, X-ray photoelectron spectroscopy (XPS) is employed here. As shown in Figs. 2d and S4, it is clear to observe that the main elements of MXene are Ti, C, O and F, originating from the oxygen-containing functional groups and F groups on the surface of the MXene after the in situ HF etching. The peaks at 35 eV, 60 eV, 456 eV and 562 eV separately correspond to the characteristic peaks of Ti 3p, Ti 3s, Ti 2p and Ti 2s. Besides, the peaks at 285 eV, 532 eV and 685 eV are assigned to C 1s, O 1s and F 1s, respectively [31].

The high-resolution XPS spectra of Ti 2p and C 1s core levels of MX/rGO-5 hybrid aerogel are shown in Fig. 2e and f. The C 1s core level is fitted with five components centered at 281.5 eV, 282.3 eV, 284.8 eV, 286.2 eV, and 288.7 eV, which assign to C–Ti, C–Ti–O/F, C–C, C–O and C=O bonds, respectively. The slight peak of C=O bond reflects the reduction of GO

in the aerogel has not fully realized [10]. The Ti 2p core level consists of three doublets (Ti 2p<sub>3/2</sub>–Ti 2p<sub>1/2</sub>). The peaks of Ti 2p<sub>3/2</sub> components locating at 455.1 eV, 456.1 eV, and 457.8 eV correspond to Ti–C, Ti (II), and Ti–O bonds, respectively [31]. Similar to other work, a shallow peak of Ti–O bond still exist, assigning to the TiO<sub>2</sub> formed by the weak oxidation of MXene [20, 32].

The SEM images of rGO aerogel and MX/rGO hybrid aerogels with a continuous three-dimensional network coupled with parallel-plane structure are presented in Fig. 3. Due to the directional extrusion of ice crystals in the ice-template method, MX/rGO-0, MX/rGO-3 and MX/rGO-5 possess anisotropic structures as indicated by the red arrow in Fig. 3a, c and e. With the increase of the MXene content, the content of rGO, which acts as a cross-linking agent, relatively decreases, so the planar-spacing becomes larger, from about 3 μm for MX/rGO-0 to about 10 μm for MX/rGO-3 (Fig. 3d) and about 12 μm for MX/rGO-5 (Fig. 3f). Interestingly, the walls of the parallel-plane structures of MX/rGO-3 and MX/rGO-5 become thicker. The thicker “wall” and larger “room” can effectively increase the multiple reflection in the hybrid aerogel, which is beneficial to enhance the

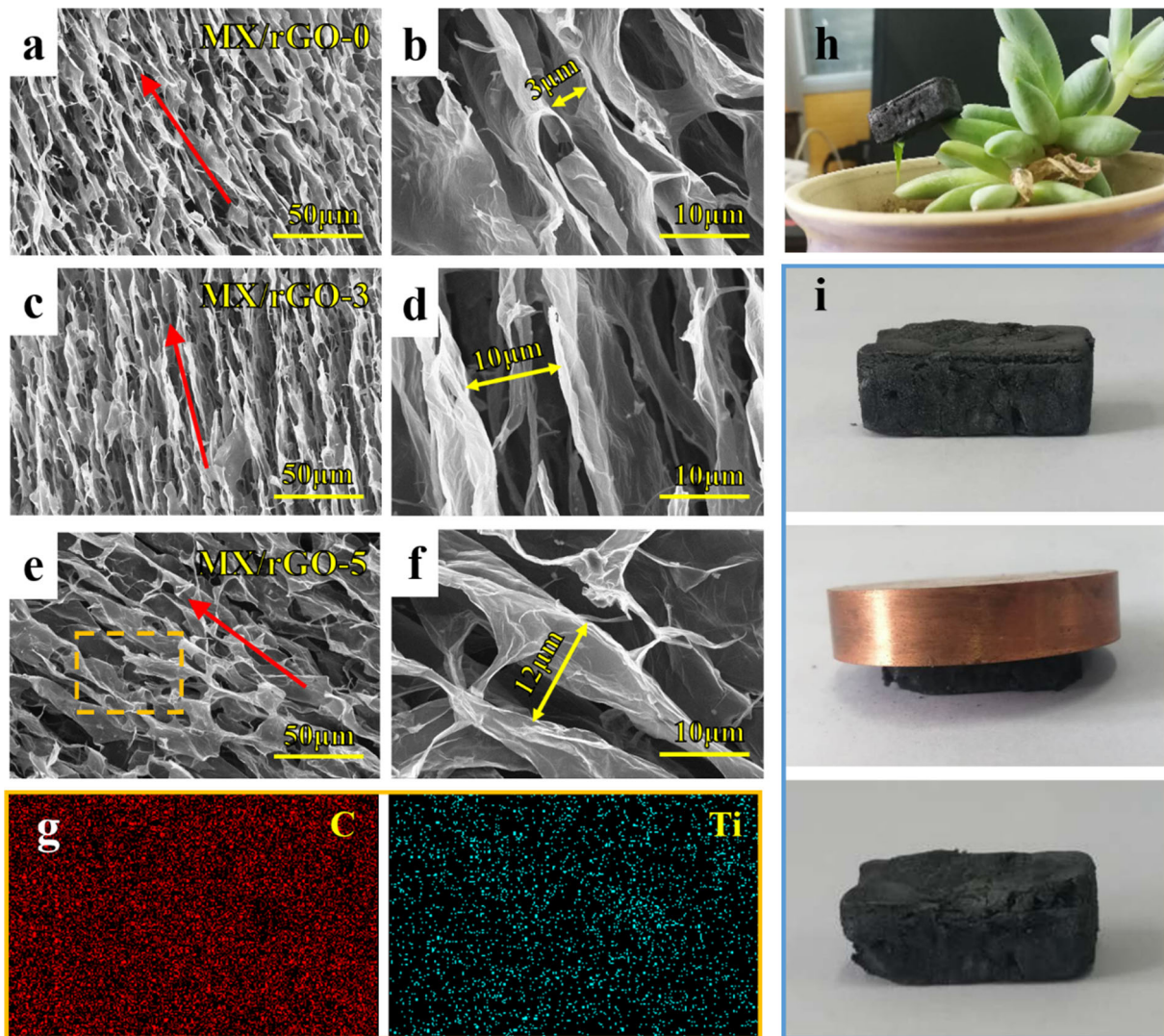


**Fig. 3** SEM images of **a, b** MX/rGO-0, **c, d** MX/rGO-3 and **e, f** MX/rGO-5 cross section. The red arrows represent the direction of the porous structure. **g** EDS diagram of the selected area in (e).

EMI shielding performance. The EDS energy spectra of MX/rGO-3 hybrid aerogel are shown in Fig. 3g, in which the Ti signals come from MXene and the C signals from MXene and rGO, respectively. The homogeneous distribution of Ti element in MX/rGO-3 elucidates that MXene have been uniformly compounded with rGO. The density of the MX/rGO-3 hybrid aerogel (25 mg) is about  $0.0104 \text{ g cm}^{-3}$ . This aerogel is light enough to steadily rest on a fleshy plant (Fig. 3h). The MX/rGO-3 hybrid aerogel exhibits excellent load capacity and resilience as shown in Fig. 3i. The MX/rGO-3 hybrid aerogel can support a copper column (70 g), which is more than 2500 times heavier than its original weight. After removing the

**h, i** Digital images of MX/rGO-3 resting on a plant, supporting a copper column with a weight of 70 g and returning to its original shape after removing the copper column (Color figure online)

copper column, the aerogel is able to return to the original brick-like shape.

### 3.2 Electrical and EMI-shielding performance of MX/rGO hybrid aerogels

The electrical and electromagnetic shielding properties of MX/rGO hybrid aerogels are shown in Fig. 4. The anisotropic structure provides a more regular electrically conductive path through the aerogels. Thus, the conductivity of MX/rGO-0 ( $142 \text{ S m}^{-1}$ ) is higher than other pure rGO foam [9]. With the addition of MXene, the conductivity of MX/rGO

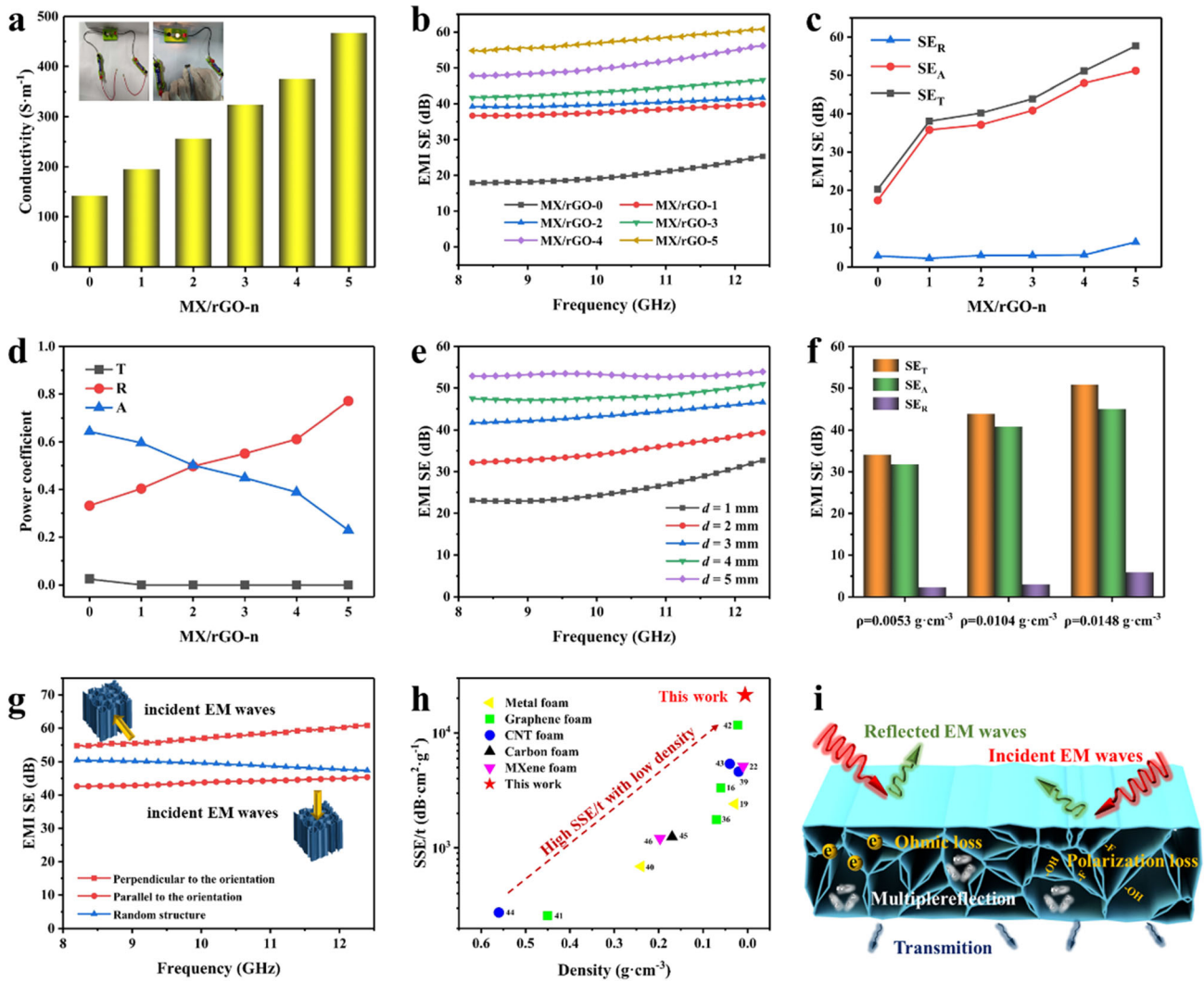


**Fig. 4** **a** Conductivity of MX/rGO hybrid aerogels with different ratios and a homemade circuit. **b** Electromagnetic shielding efficiency, **c** average  $SE_T$ ,  $SE_A$ ,  $SE_R$  and **d**  $T$ ,  $R$  and  $A$  coefficient of MX/rGO hybrid aerogels with a thickness of 3 mm. **e** Electromagnetic shielding effectiveness of MX/rGO-3 hybrid aerogels with different thickness. **f** Comparison of  $SE_T$ ,  $SE_R$  and  $SE_R$  of MX/rGO-3 hybrid aerogels with different density.

hybrid aerogels gradually increases. As for MX/rGO-5, the conductivity reaches as high as  $467 \text{ S m}^{-1}$ , and its low resistivity allows the bulb in the circuit to light normally (Fig. 4a).

Furthermore, the conductivity also contributes to the electromagnetic shielding performance. As shown in Fig. 4b, with the increase of MXene, the EMI SE of MX/rGO hybrid aerogels exhibits an obvious increasement from 38.07 to 57.67 dB, which is higher than 20.29 dB of MX/rGO-0 aerogel. Meanwhile, the porous structures provide more

**g** EMI shielding performances of MX/rGO-5 with different structures when the incident EM waves come from different directions. **h** Comparison of the  $SSE/t$  as a function of density for various foam-like materials. The numbers inside the figure are the reference numbers listed in Table 1. **i** A schematic diagram of the possible EMI shielding mechanism of MX/rGO-5 hybrid aerogel

effective interfaces to reflect and attenuate the incident electromagnetic wave, which promotes the electromagnetic shielding effectiveness of the hybrid aerogels. As for 3-mm-thick MX/rGO-5 hybrid aerogel, the shielding performance reaches 57.67 dB, showing a high capability to block 99.9998% of incident waves and only 0.0002% transmission, far exceeds the target value for commercial application (20 dB). The detailed data of electrical conductivity and EMI SE of MX/rGO hybrid aerogels are listed in Table S1.

Both  $SE_T$  and  $SE_A$  increase obviously with the loading of MXene in Fig. 4c, whereas  $SE_R$  increases only slightly and is always lower than  $SE_A$ . The increase of  $SE_T$  with the loading of MXene principally comes from the contribution of  $SE_A$ . For example, the average  $SE_R$ ,  $SE_A$ , and  $SE_T$  in X band of the MX/rGO-5 are 6.46, 51.21, and 57.67 dB, respectively. About 88.8% of the incident electromagnetic wave is attenuated by the electromagnetic absorption. It is important to note that the absorption occurs after the reflection by the material, so that  $SE_A$  only denotes the ability of shielding material to attenuate electromagnetic waves that have already transmitted into the material [14].

According to the above formula (1–3), the  $T$ ,  $A$  and  $R$  coefficient, which signify the power balance of electromagnetic waves interacting with the shielding materials, are calculated from  $S_{11}$  and  $S_{21}$  parameters [33]. As shown in Fig. 4d, the  $R$  coefficient increases with the increasing MXene mass ratio, while  $A$  coefficient declines. The presence of MXene brings more free electron on the surface of MX/rGO hybrid aerogel, and the better electrical conductivity results in the impedance mismatch at interfaces [34]. As for MX/rGO-0 and MX/rGO-1, the  $A$  is higher than  $R$ , indicating that the dominant shielding mechanism of them is absorption. While the  $A$  is lower than  $R$  in MX/rGO-3, MX/rGO-4 and MX/rGO-5, so that the more decisive shielding mechanism of them is reflection because of their excellent electrical conductivity. Therefore, the dominant mechanism of electromagnetic shielding of MX/rGO aerogels is dependent on the MXene mass ratio.

Apart from the ratio of MXene, the shielding materials' thickness is another vital factor that influences the electromagnetic shielding performance. As the thickness of the shielding material increases, the electromagnetic waves will be absorbed, attenuated and reflected more times in the shielding materials. Therefore, the thicker the aerogels are, the higher the electromagnetic shielding performance of MX/rGO-3 hybrid aerogel is, as shown in Fig. 4e. For example, the average EMI SE of MX/rGO-3 hybrid aerogel with 5 mm thickness in X band reaches up to 53.09 dB, which is much higher than the 1-mm-thick hybrid aerogel (26.21 dB).

By changing the concentration of the MX/GO solution, MX/rGO-3 hybrid aerogels with different density (i.e.,  $0.0053 \text{ g cm}^{-3}$ ,  $0.0104 \text{ g cm}^{-3}$ ,  $0.0148 \text{ g cm}^{-3}$ ) were also prepared, and their  $SE_T$ ,  $SE_A$  and  $SE_R$

are shown in Fig. 4f. Apparently, the electromagnetic shielding performance becomes higher with the increase of density, and their main shielding factor is still the absorption effect. The aerogels with the increased density give rise to the decrease of the pore diameter, but enrich the quantity of pores in hybrid aerogels. A higher density of the porous structure enhances the perfection of the conductive network in the MX/rGO hybrid aerogels, so that the electromagnetic shielding performance is highly improved.

As for the hybrid aerogels with anisotropic structure, it is necessary to measure the EMI shielding performance from different directions. In Fig. 4g, the average EMI SE perpendicular to the orientation (57.67 dB) is better than that parallel to the orientation (42.24 dB), because there are more MXene and rGO nanosheets distributed along the orientation direction. Meanwhile, we prepared by ordinary freezing method a random-structured hybrid aerogel (with the same ratio as MX/rGO-5), in which the nanosheets are freely distributed (as shown in Fig. S5), and the average EMI SE (50.04 dB) falls in the middle. These results further indicate that the hybrid aerogels with anisotropic structures demonstrate the anisotropic electromagnetic shielding properties. The underlying electromagnetic shielding mechanism will be studied in the future.

To eliminate the effects of thickness, the results of SSE divided by the sample thickness ( $SSE/t$ ) [35] are summarized in Fig. 4 h and 1. Traditionally, the foam-like materials consisting of metals, CNTs or graphene are promising for EMI shielding applications. For example, the  $SSE/t$  of a graphene aerogel is  $1763 \text{ dB cm}^2 \text{ g}^{-1}$ , and a CNT-sponge is  $4621 \text{ dB cm}^2 \text{ g}^{-1}$  [36, 37]. In this work, the  $SSE/t$  of MX/rGO-3 hybrid aerogels reaches as high as  $21,427 \text{ dB cm}^2 \text{ g}^{-1}$ , higher than most of the shielding materials reported so far. To better elucidate the EMI shielding mechanism of MX/rGO-5 hybrid aerogel, a schematic diagram of the possible paths of electromagnetic waves across the aerogel is shown in Fig. 4i. The abundant free electrons on the surface of MX/rGO hybrid aerogels give themselves a lot of paths with high conductivity. When the incident electromagnetic waves reach the surface of the aerogel, a part of electromagnetic waves will be reflected immediately. After the remaining electromagnetic waves enter the aerogels, when they passing through the conductive 3D network, it will result in ohmic loss and reducing their energy. Meanwhile, multiple absorption



**Table 1** Comparison of EMI shielding performance for foam-like various materials

Materials	Thickness (cm)	Density (g cm <sup>-3</sup> )	EMI SE (dB)	SSE (dB cm <sup>3</sup> g <sup>-1</sup> )	SSE/ <i>t</i> (dB cm <sup>2</sup> g <sup>-1</sup> )	References
CuNi	0.15	0.24	25	104	690	[40]
AgNW/PI	0.5	0.029	35	1208	2416	[19]
rGO/PDMS	0.1	0.06	20	333	3330	[16]
Graphene aerogel	0.3	0.07	37	529	1763	[36]
Graphene/PS	0.2	0.45	29	64.4	258	[41]
Graphene/PI	0.08	0.022	21	937	11,712	[42]
CNT-sponge	0.24	0.02	22	1100	4621	[37]
MWCNT/WPU	0.1	0.04	21	541	5410	[43]
SWCNT/PS	0.12	0.56	18.5	33	275	[44]
Carbon foam	0.2	0.17	40	241	1250	[45]
MXene/WPC	0.3	0.197	71	362	1207	[46]
MXene/PVA	0.5	0.01	28	2586	5136	[22]
MX/rGO-3	0.3	0.0053	34	6428	21,427	This work

attenuation and reflection consumption will occur within the inner porous structures. In addition, the surface functional groups, heterogeneous interfaces and structural defects between the MXene and rGO provide various dipole polarizations, which further attenuates the incident electromagnetic wave [38, 39]. Eventually, the electromagnetic waves are dissipated in the form of heat in the MX/rGO hybrid aerogels.

## 4 Conclusions

A lightweight MX/rGO hybrid aerogel with superior electrical conductivity and EMI performance has been successfully prepared in this work. The MX/GO aerogels with continuous and stable network structures were constructed by unidirectional freezing and freeze-drying. Then, the mild chemical reduction treatment using HI and HAc mixture effectively reduced GO and avoided MXene from being hugely oxidated. The MX/rGO-5 hybrid aerogel exhibited an optimal electrical conductivity of 467 S m<sup>-1</sup>, and the maximum EMI SE value of 57.67 dB (average in X-band). The SSE/*t* of MX/rGO-3 hybrid aerogel with a low density reaches as high as 21,427 cm<sup>2</sup> g<sup>-1</sup>. The mild chemical reduction treatment guaranteed the remarkable electrical property, EMI shielding performance and SSE/*t* of MX/rGO hybrid aerogels. This work provides a new strategy for the fabrication of lightweight and efficient 3D electromagnetic shielding materials.

## Acknowledgements

The authors gratefully acknowledge the financial support of this work by the National Natural Science Foundation of China (Grant Nos. 21978240, 21676217, 52003219, 51503170), Youth project of basic research program of Natural Science in Shaanxi Province (Grant No. 2020JQ-179), Ningbo Natural Science Foundation (Grant No. 202003N4370) the Fundamental Research Funds for the Central Universities, the Seed Foundation of Innovation and Creation for Graduate Students in Northwestern Polytechnical University (Grant No. CX2020218), and the Open Testing Foundation of the Analytical & Testing Center of Northwestern Polytechnical University (Grant No. 2020T020).

## Author contribution

All authors contributed to the study conception and design. Material preparation, data collection and analysis were performed by Haiyang Li, Yiwen Peng, Zewen Fan, Junjie Feng. Project administration and supervision were performed by Lei Gong, Zhen-guo Liu, Qiuyu Zhan. The first draft of the manuscript was written by Xuanhe Ru, reviewed and edited by Yanhui Chen. All authors commented on previous versions of the manuscript. All authors read and approved the final manuscript.

## Data availability

The authors confirm that the data supporting the findings of this study are available within the article.

## Declarations

The authors declare that they have no known competing financial interests or personal relationships that could have appeared to influence the work reported in this paper.

**Conflict of interest** The authors have no relevant financial or non-financial interests to disclose.

**Supplementary Information:** The online version contains supplementary material available at <https://doi.org/10.1007/s10854-021-07603-w>.

## References

- M.H. Al-Saleh, U. Sundararaj, *Carbon* **47**, 1738 (2009). <https://doi.org/10.1016/j.carbon.2009.02.030>
- N. Yousefi, X. Sun, X. Lin et al., *Adv. Mater.* **26**, 5480 (2014). <https://doi.org/10.1002/adma.201305293>
- M. Ghidui, M.R. Lukatskaya, M.Q. Zhao, Y. Gogotsi, M.W. Barsoum, *Nature* **516**, 78 (2014). <https://doi.org/10.1038/nature13970>
- L. Li, M. Zhang, X. Zhang, Z. Zhang, *J. Power Sources* **364**, 234 (2017). <https://doi.org/10.1016/j.jpowsour.2017.08.029>
- Y. Yue, N. Liu, Y. Ma et al., *ACS Nano* **12**, 4224 (2018). <https://doi.org/10.1021/acs.nano.7b07528>
- M. Naguib, J. Come, B. Dyatkin et al., *Electrochem. Commun.* **16**, 61 (2012). <https://doi.org/10.1016/j.elecom.2012.01.002>
- Y.T. Liu, P. Zhang, N. Sun et al., *Adv Mater* **30**, e1707334 (2018). <https://doi.org/10.1002/adma.201707334>
- R. Bian, G. He, W. Zhi, S. Xiang, T. Wang, D. Cai, *J. Mater. Chem. C* **7**, 474 (2019). <https://doi.org/10.1039/c8tc04795b>
- Z. Fan, D. Wang, Y. Yuan et al., *Chem. Eng. J.* (2020). <https://doi.org/10.1016/j.cej.2019.122696>
- S. Zhao, H.B. Zhang, J.Q. Luo et al., *ACS Nano* **12**, 11193 (2018). <https://doi.org/10.1021/acs.nano.8b05739>
- F. Shahzad, M. Alhabeib, C.B. Hatter et al., *Science* **353**, 1137 (2016). <https://doi.org/10.1126/science.aag2421>
- X. Jin, J. Wang, L. Dai et al., *Chem. Eng. J.* (2020). <https://doi.org/10.1016/j.cej.2019.122475>
- B. Wen, M. Cao, M. Lu et al., *Adv. Mater.* **26**, 3484 (2014). <https://doi.org/10.1002/adma.201400108>
- Q. Song, F. Ye, X. Yin et al., *Adv. Mater.* (2017). <https://doi.org/10.1002/adma.201701583>
- M.-S. Cao, Y.-Z. Cai, P. He, J.-C. Shu, W.-Q. Cao, J. Yuan, *Chem. Eng. J.* **359**, 1265 (2019). <https://doi.org/10.1016/j.cej.2018.11.051>
- Z. Chen, C. Xu, C. Ma, W. Ren, H.M. Cheng, *Adv. Mater.* **25**, 1296 (2013). <https://doi.org/10.1002/adma.201204196>
- C.-H. Cui, D.-X. Yan, H. Pang et al., *Chem. Eng. J.* **323**, 29 (2017). <https://doi.org/10.1016/j.cej.2017.04.050>
- M.Q. Zhao, X. Xie, C.E. Ren et al., *Adv. Mater.* (2017). <https://doi.org/10.1002/adma.201702410>
- J. Liu, H.B. Zhang, R. Sun et al., *Adv. Mater.* (2017). <https://doi.org/10.1002/adma.201702367>
- C.J. Zhang, S. Pinilla, N. McEyoy et al., *Chem. Mater.* **29**, 4848 (2017). <https://doi.org/10.1021/acs.chemmater.7b00745>
- J. Liu, H.B. Zhang, X. Xie et al., *Small* **14**, e1802479 (2018). <https://doi.org/10.1002/sml.201802479>
- H. Xu, X. Yin, X. Li et al., *ACS Appl. Mater. Interfaces* **11**, 10198 (2019). <https://doi.org/10.1021/acsami.8b21671>
- Z. Zhou, J. Liu, X. Zhang, D. Tian, Z. Zhan, C. Lu, *Adv. Mater. Interfaces* (2019). <https://doi.org/10.1002/admi.201802040>
- D.R. Dreyer, S. Park, C.W. Bielawski, R.S. Ruoff, *Chem. Soc. Rev.* **39**, 228 (2010). <https://doi.org/10.1039/b917103g>
- H.-P. Cong, J.-F. Chen, S.-H. Yu, *Chem. Soc. Rev.* **43**, 7295 (2014). <https://doi.org/10.1039/c4cs00181h>
- T. Zhou, C. Wu, Y. Wang et al., *Nat. Commun.* **11**, 2077 (2020). <https://doi.org/10.1038/s41467-020-15991-6>
- W. Cao, C. Ma, S. Tan, M. Ma, P. Wan, F. Chen, *Nano-Micro Lett.* (2019). <https://doi.org/10.1007/s40820-019-0304-y>
- C. Cui, C. Xiang, L. Geng et al., *J. Alloys Compd.* **788**, 1246 (2019). <https://doi.org/10.1016/j.jallcom.2019.02.294>
- D.-X. Yan, H. Pang, B. Li et al., *Adv. Funct. Mater.* **25**, 559 (2015). <https://doi.org/10.1002/adfm.201403809>
- J. Yan, C.E. Ren, K. Maleski et al., *Adv. Funct. Mater.* (2017). <https://doi.org/10.1002/adfm.201701264>
- R.P. Pandey, K. Rasool, V.E. Madhavan, B. Aissa, Y. Gogotsi, K.A. Mahmoud, *J. Mater. Chem. A* **6**, 3522 (2018). <https://doi.org/10.1039/c7ta10888e>
- X. Jia, B. Shen, L. Zhang, W. Zheng, *Composites Part B Eng.* (2020). <https://doi.org/10.1016/j.compositesb.2020.108250>
- Y.-J. Wan, P.-L. Zhu, S.-H. Yu, R. Sun, C.-P. Wong, W.-H. Liao (2018) *Small* **14**. <https://doi.org/10.1002/sml.201800534>
- F. Ren, D. Song, Z. Li et al., *J. Mater. Chem. C* **6**, 1476 (2018). <https://doi.org/10.1039/c7tc05213h>
- Z. Zeng, H. Jin, M. Chen et al., *Small* (2017). <https://doi.org/10.1002/sml.201701388>

36. W.-L. Song, X.-T. Guan, L.-Z. Fan, W.-Q. Cao, C.-Y. Wang, M.-S. Cao, *Carbon* **93**, 151 (2015). <https://doi.org/10.1016/j.carbon.2015.05.033>
37. M. Crespo, M. Gonzalez, A.L. Elias et al., *Physica Status Solidi Rapid Res. Lett.* **8**, 698 (2014). <https://doi.org/10.1002/pssr.201409151>
38. R. Sun, H.-B. Zhang, J. Liu et al., *Adv. Funct. Mater.* (2017). <https://doi.org/10.1002/adfm.201702807>
39. X. Li, X. Yin, M. Han et al., *J. Mater. Chem. C* **5**, 7621 (2017). <https://doi.org/10.1039/c7tc01991b>
40. K. Ji, H. Zhao, J. Zhang, J. Chen, Z. Dai, *Appl. Surf. Sci.* **311**, 351 (2014). <https://doi.org/10.1016/j.apsusc.2014.05.067>
41. D.-X. Yan, P.-G. Ren, H. Pang, Q. Fu, M.-B. Yang, Z.-M. Li, *J. Mater. Chem.* (2012). <https://doi.org/10.1039/c2jm32692b>
42. Y. Li, X. Pei, B. Shen, W. Zhai, L. Zhang, W. Zheng, *RSC Adv.* **5**, 24342 (2015). <https://doi.org/10.1039/c4ra16421k>
43. Z. Zeng, H. Jin, M. Chen, W. Li, L. Zhou, Z. Zhang, *Adv. Funct. Mater.* **26**, 303 (2016). <https://doi.org/10.1002/adfm.201503579>
44. Y.L. Yang, M.C. Gupta, *Nano Lett.* **5**, 2131 (2005). <https://doi.org/10.1021/nl051375r>
45. F. Moglie, D. Micheli, S. Laurenzi, M. Marchetti, V.M. Primiani, *Carbon* **50**, 1972 (2012). <https://doi.org/10.1016/j.carbon.2011.12.053>
46. C. Liang, H. Qiu, P. Song, X. Shi, J. Kong, J. Gu, *Sci. Bull.* **65**, 616 (2020). <https://doi.org/10.1016/j.scib.2020.02.009>

**Publisher's Note** Springer Nature remains neutral with regard to jurisdictional claims in published maps and institutional affiliations.